Biomedical Optics EXPRESS

Optical coherence tomography detection of shear wave propagation in inhomogeneous tissue equivalent phantoms and *ex-vivo* carotid artery samples

Marjan Razani,[1] Timothy W.H. Luk,[2] Adrian Mariampillai,[2] Peter Siegler,[2] Tim-Rasmus Kiehl,[4,5] Michael C. Kolios,[1,6] and Victor X.D. Yang,[1,2,3,7]

[1]*Department of Physics, Ryerson University, Toronto, Canada*
[2]*Department of Electrical and Computer Engineering, Ryerson University, Toronto, Canada*
[3]*Division of Neurosurgery, University of Toronto, Toronto, Canada*
[4]*Department of Pathology, University Health Network, Toronto, Ontario Canada*
[5]*Department of Laboratory Medicine and Pathobiology, University of Toronto, Ontario, Canada*
[6]*mkolios@ryerson.ca*
[7]*victor.yang@sunnybrook.ca*

Abstract: In this work, we explored the potential of measuring shear wave propagation using optical coherence elastography (OCE) in an inhomogeneous phantom and carotid artery samples based on a swept-source optical coherence tomography (OCT) system. Shear waves were generated using a piezoelectric transducer transmitting sine-wave bursts of 400 μs duration, applying acoustic radiation force (ARF) to inhomogeneous phantoms and carotid artery samples, synchronized with a swept-source OCT (SS-OCT) imaging system. The phantoms were composed of gelatin and titanium dioxide whereas the carotid artery samples were embedded in gel. Differential OCT phase maps, measured with and without the ARF, detected the microscopic displacement generated by shear wave propagation in these phantoms and samples of different stiffness. We present the technique for calculating tissue mechanical properties by propagating shear waves in inhomogeneous tissue equivalent phantoms and carotid artery samples using the ARF of an ultrasound transducer, and measuring the shear wave speed and its associated properties in the different layers with OCT phase maps. This method lays the foundation for future *in-vitro* and *in-vivo* studies of mechanical property measurements of biological tissues such as vascular tissues, where normal and pathological structures may exhibit significant contrast in the shear modulus.

OCIS codes: (170.4500) Optical coherence tomography; (170.6935) Tissue characterization.

References and links

1. J. Ophir, S. K. Alam, B. Garra, F. Kallel, E. Konofagou, T. Krouskop, and T. Varghese, "Elastography: ultrasonic estimation and imaging of the elastic properties of tissues," Proc. Inst. Mech. Eng. H **213**(3), 203–233 (1999).
2. C. Sun, B. Standish, and V. X. D. Yang, "Optical coherence elastography: current status and future applications," J. Biomed. Opt. **16**(4), 043001 (2011).
3. F. Sebag, J. Vaillant-Lombard, J. Berbis, V. Griset, J. F. Henry, P. Petit, and C. Oliver, "Shear wave elastography: a new ultrasound imaging mode for the differential diagnosis of benign and malignant thyroid nodules," J. Clin. Endocrinol. Metab. **95**(12), 5281–5288 (2010).
4. R. Z. Slapa, A. Piwowonski, W. S. Jakubowski, J. Bierca, K. T. Szopinski, J. Slowinska-Srzednicka, B. Migda, and R. K. Mlosek, "Shear wave elastography may add a new dimension to ultrasound evaluation of thyroid nodules: case series with comparative evaluation," J. Thyroid Res. **2012**, 657147 (2012).
5. G. Scarcelli and S. H. Yun, "Confocal Brillouin microscopy for three-dimensional mechanical imaging," Nat. Photonics **2**(1), 39–43 (2008).

#200332 - $15.00 USD Received 4 Nov 2013; revised 16 Jan 2014; accepted 19 Feb 2014; published 26 Feb 2014

6. S. Shah, M. Laiquzzaman, R. Bhojwani, S. Mantry, and I. Cunliffe, "Assessment of the biomechanical properties of the cornea with the ocular response analyzer in normal and keratoconic eyes," Invest. Ophthalmol. Vis. Sci. **48**(7), 3026–3031 (2007).
7. J. Li, S. Wang, R. K. Manapuram, M. Singh, F. M. Menodiado, S. Aglyamov, S. Emelianov, M. D. Twa, and K. V. Larin, "Dynamic optical coherence tomography measurements of elastic wave propagation in tissue-mimicking phantoms and mouse cornea in vivo," J. Biomed. Opt. **18**(12), 121503 (2013).
8. J. M. Schmitt, "OCT elastography: imaging microscopic deformation and strain of tissue," Opt. Express **3**(6), 199–211 (1998).
9. X. Liang, M. Orescanin, K. S. Toohey, M. F. Insana, and S. A. Boppart, "Acoustomotive optical coherence elastography for measuring material mechanical properties," Opt. Lett. **34**(19), 2894–2896 (2009).
10. J. F. Greenleaf, M. Fatemi, and M. Insana, "Selected methods for imaging elastic properties of biological tissues," Annu. Rev. Biomed. Eng. **5**(1), 57–78 (2003).
11. J. G. Fujimoto, M. E. Brezinski, G. J. Tearney, S. A. Boppart, B. E. Bouma, M. R. Hee, J. F. Southern, and E. A. Swanson, "Optical biopsy and imaging using optical coherence tomography," Nat. Med. **1**(9), 970–972 (1995).
12. S. Song, Z. Huang, and R. K. Wang, "Tracking mechanical wave propagation within tissue using phase-sensitive optical coherence tomography: Motion artifact and its compensation," J. Biomed. Opt. **18**(12), 121505 (2013).
13. S. Wang, S. Aglyamov, A. Karpiouk, J. Li, S. Emelianov, F. Manns, and K. V. Larin, "Assessing the mechanical properties of tissue-mimicking phantoms at different depths as an approach to measure biomechanical gradient of crystalline lens," Biomed. Opt. Express **4**(12), 2769–2780 (2013).
14. A. P. Sarvazyan, O. V. Rudenko, S. D. Swanson, J. B. Fowlkes, and S. Y. Emelianov, "Shear wave elasticity imaging: A new ultrasonic technology of medical diagnostics," Ultrasound Med. Biol. **24**(9), 1419–1435 (1998).
15. M. F. O'Rourke, J. A. Staessen, C. Vlachopoulos, D. Duprez, and G. E. Plante, "Clinical applications of arterial stiffness; definitions and reference values," Am. J. Hypertens. **15**(5), 426–444 (2002).
16. K. S. Cheng, C. R. Baker, G. Hamilton, A. P. G. Hoeks, and A. M. Seifalian, "Arterial elastic properties and cardiovascular risk/event," Eur. J. Vasc. Endovasc. Surg. **24**(5), 383–397 (2002).
17. S. Laurent, P. Boutouyrie, R. Asmar, I. Gautier, B. Laloux, L. Guize, P. Ducimetiere, and A. Benetos, "Aortic stiffness is an independent predictor of all-cause and cardiovascular mortality in hypertensive patients," Hypertension **37**(5), 1236–1241 (2001).
18. M. Couade, M. Pernot, C. Prada, E. Messas, J. Emmerich, P. Bruneval, A. Criton, M. Fink, and M. Tanter, "Quantitative assessment of arterial wall biomechanical properties using shear wave imaging," Ultrasound Med. Biol. **36**(10), 1662–1676 (2010).
19. G. Pasterkamp and E. Falk, "Atherosclerotic plaque rupture: an overview," J. Clin. Basic Cardiol. **3**, 81–86 (2000).
20. E. Falk, "Why do plaques rupture?" Circulation **86**(6 Suppl), III30–III42 (1992).
21. K. C. Hilty and D. H. Steinberg, "Vulnerable plaque imaging-current techniques," J. Cardiovasc. Transl. Res. **2**(1), 9–18 (2009).
22. F. Sharif and R. T. Murphy, "Current status of vulnerable plaque detection," Catheter. Cardiovasc. Interv. **75**(1), 135–144 (2010).
23. C. Schmitt, G. Soulez, R. L. Maurice, M. F. Giroux, and G. Cloutier, "Noninvasive vascular elastography: toward a complementary characterization tool of atherosclerosis in carotid arteries," Ultrasound Med. Biol. **33**(12), 1841–1858 (2007).
24. J. J. Dahl, D. M. Dumont, J. D. Allen, E. M. Miller, and G. E. Trahey, "Acoustic radiation force impulse imaging for noninvasive characterization of carotid artery atherosclerotic plaques: a feasibility study," Ultrasound Med. Biol. **35**(5), 707–716 (2009).
25. M. Fatemi and J. F. Greenleaf, "Application of radiation force in noncontact measurement of the elastic parameters," Ultrason. Imaging **21**(2), 147–154 (1999).
26. M. Elkateb Hachemi, S. Callé, and J. P. Remenieras, "Transient displacement induced in shear wave elastography: comparison between analytical results and ultrasound measurements," Ultrasonics **44**(Suppl 1), e221–e225 (2006).
27. L. Ostrovsky, A. Sutin, Y. Il'inskii, O. Rudenko, and A. Sarvazyan, "Radiation force and shear motions in inhomogeneous media," J. Acoust. Soc. Am. **121**(3), 1324–1331 (2007).
28. M. L. Palmeri, S. A. McAleavey, K. L. Fong, G. E. Trahey, and K. R. Nightingale, "Dynamic mechanical response of elastic spherical inclusions to impulsive acoustic radiation force excitation," IEEE Trans. Ultrason. Ferroelectr. Freq. Control **53**(11), 2065–2079 (2006).
29. W. F. Walker, F. J. Fernandez, and L. A. Negron, "A method of imaging viscoelastic parameters with acoustic radiation force," Phys. Med. Biol. **45**(6), 1437–1447 (2000).
30. K. Nightingale, M. S. Soo, R. Nightingale, and G. Trahey, "Acoustic radiation force impulse imaging: In vivo demonstration of clinical feasibility," Ultrasound Med. Biol. **28**(2), 227–235 (2002).
31. S. H. Yun, G. J. Tearney, J. F. de Boer, and B. E. Bouma, "Motion artifacts in optical coherence tomography with frequency-domain ranging," Opt. Express **12**(13), 2977–2998 (2004).
32. K. R. Nightingale, R. W. Nightingale, D. L. Stutz, and G. E. Trahey, "Acoustic radiation force impulse imaging of in vivo vastus medialis muscle under varying isometric load," Ultrason. Imaging **24**(2), 100–108 (2002).
33. M. Fatemi and J. F. Greenleaf, "Ultrasound-stimulated vibro-acoustic spectrography," Science **280**(5360), 82–85 (1998).

#200332 - $15.00 USD Received 4 Nov 2013; revised 16 Jan 2014; accepted 19 Feb 2014; published 26 Feb 2014

34. J. D. Allen, K. L. Ham, D. M. Dumont, B. Sileshi, G. E. Trahey, and J. J. Dahl, "The development and potential of acoustic radiation force impulse (ARFI) imaging for carotid artery plaque characterization," Vasc. Med. **16**(4), 302–311 (2011).
35. M. Razani, A. Mariampillai, C. Sun, T. W. H. Luk, V. X. D. Yang, and M. C. Kolios, "Feasibility of optical coherence elastography measurements of shear wave propagation in homogeneous tissue equivalent phantoms," Biomed. Opt. Express **3**(5), 972–980 (2012).
36. D. C. Adler, R. Huber, and J. G. Fujimoto, "Phase-sensitive optical coherence tomography at up to 370,000 lines per second using buffered Fourier domain mode-locked lasers," Opt. Lett. **32**(6), 626–628 (2007).
37. M. W. Urban and J. F. Greenleaf, "A Kramers-Kronig-based quality factor for shear wave propagation in soft tissue," Phys. Med. Biol. **54**(19), 5919–5933 (2009).
38. C. Amador, M. W. Urban, S. Chen, Q. Chen, K.-N. An, and J. F. Greenleaf, "Shear elastic modulus estimation from indentation and SDUV on gelatin phantoms," IEEE Trans. Biomed. Eng. **58**(6), 1706–1714 (2011).
39. V. X. D. Yang, M. L. Gordon, B. Qi, J. Pekar, S. Lo, E. Seng-Yue, A. Mok, B. C. Wilson, and I. A. Vitkin, "High speed, wide velocity dynamic range Doppler optical coherence tomography (Part I): System design, signal processing, and performance," Opt. Express **11**(7), 794–809 (2003).
40. S. Le Floc'h, G. Cloutier, G. Finet, P. Tracqui, R. I. Pettigrew, and J. Ohayon, "On the potential of a new IVUS elasticity modulus imaging approach for detecting vulnerable atherosclerotic coronary plaques: in vitro vessel phantom study," Phys. Med. Biol. **55**(19), 5701–5721 (2010).
41. H. Kanai, H. Hasegawa, M. Ichiki, F. Tezuka, and Y. Koiwa, "Elasticity imaging of atheroma with transcutaneous ultrasound: preliminary study," Circulation **107**(24), 3018–3021 (2003).

1. Introduction

Elastography is a method for analyzing the biomechanical properties of tissues based on stiffness and strain images [1]. The biomaterial tissue deformations caused by static or dynamic loads are recorded in elastograms that contain data about the local variations of the stiffness inside a region of interest [2]. This information is valuable for identifying and assessing biomaterial variations of the target tissue. The shear modulus of biomaterials in particular is thought to be highly sensitive to variations in the biomaterial properties. There are many different imaging modalities that can be used to measure displacements and estimate the resulting mechanical properties. Two of these are ultrasound (US) and magnetic resonance imaging (MRI). However, they come with significant drawbacks, such as high cost and complex design. They also have insufficient spatial resolution to detect small scale and subtle elastic variations in biomaterials and tissues, such as in tissue engineered modules and atherosclerotic plaques. Supersonic shear weave elastography, which is a method that uses a shear source moving through the medium at a supersonic speed (greater than the speed of the shear wave in tissue) and is use to generate parametric images of shear modulus. This can be achieved by successively focusing the ultrasonic "pushing" ARF beam at different depths at a speed that is greater than the tissue shear wave speed. The result of the beam traveling faster than the shear wave is that all the resulting shear waves interfere constructively along a Mach cone creating planes of intense shear waves propagating in opposite directions, analogous to a "sonic boom" created by a supersonic aircraft [3,4]. A method based on Brillouin light-scattering and involving a spectral shift proportional to the longitudinal modulus of elasticity of the tissue allows for non-contact and direct readout of the viscoelastic properties of a material [5]. Other methods previously investigated to compare hysteresis in normal and keratoconic eyes using the Ocular Response Analyzer (ORA; Reichert Ophthalmic Instruments, Buffalo, NY). This device is an adaptation to the noncontact tonometer (NCT) to measure the viscoelastic properties of the eye [6]. Lastly, another method uses a focused air-pulse system and a phase-stabilized swept-source optical coherence tomography to assess the propagation of low-amplitude (micron-level) waves [7].

In contrast, optical coherence tomography (OCT) has several advantages over other imaging modalities. Analogous to US, OCT uses light instead of sound waves, is inexpensive compared to other imaging modalities and has higher resolution and motion sensitivity to allow for improved identification of micron-sized morphological tissue structures and highly localized strains [8–10]. The main disadvantage of the technique is its limited penetration depth, on the order of few millimeters [11].

#200332 - $15.00 USD Received 4 Nov 2013; revised 16 Jan 2014; accepted 19 Feb 2014; published 26 Feb 2014

Optical coherence elastography (OCE) is a technique that uses OCT for measuring the biomechanical properties of soft tissues [12, 13]. The tissues can be excited internally or externally, and statically or dynamically. A common method for creating dynamic compressions for the tissue is using acoustic radiation force (ARF) or low-frequency vibrations with a needle. Shear waves generated from the application of ARF will propagate away from the initial region of excitation (i.e. the focal spot region) [14]. Typical values for the shear wave propagation speed in soft tissues range from 1 to 10 m/s and the attenuation coefficient is two to three orders of magnitude greater than that of compression waves [14]. Both of these parameters are directly related to the mechanical properties of the tissue. Due to its high attenuation, the shear wave generated propagates within a limited area of tissue, typically a few millimeters from the location of the excitation [14]. The frequency of the shear wave will be determined primarily by the width of the ultrasound beam and not the time duration of the excitation, unless the excitation duration approaches the natural time constants of soft tissue relaxation.

The study of the mechanical properties of arteries is critical to understanding cardiovascular function and in the diagnosis of vascular disease [15]. Arterial stiffness increases with aging and can be used as an indicator for cardiovascular morbidity and mortality, as well as a measure for the risk of stroke and myocardial infarction [16–18]. These acute cardiovascular events typically occur when there is a rupture of the fibrous cap of the atherosclerotic plaque, causing the formation of a thrombus that obstructs an artery [19,20]. An atherosclerotic plaque includes a large extracellular necrotic core and a thin fibrous cap infiltrated by macrophages [21, 22]. These components have properties that are important in quantifying lesion stability [23]. Specific to the carotid artery, atherosclerotic disease and plaque rupture are risk factors for stroke. ARF imaging can be applied to carotid artery samples to determine the feasibility of noninvasively characterizing atherosclerotic plaques [24].

In this work, we explore the potential for measuring shear wave propagation in inhomogeneous phantoms and excised carotid artery samples using OCT as an imaging modality to detect the shear wave propagation. Using OCE allows for the measurement of tissue displacement to generate high-resolution elastograms.

2. Materials and methods

ARF was used as the internal mechanical excitation to send focused ultrasound beams to produce the desired shear waves. The ARF was applied using a 20 MHz, circular, piezoelectric transducer element (PZT, f-number 2.35) transmitting sine-wave bursts of 400 μs duration. The internal displacements induced by the shear waves were detected using a Thorlabs swept source OCT system and phase sensitive motion detection algorithms. The OCT laser had a center wavelength of a 1310 nm, a bandwidth of ~110 nm, and an A-scan rate of 8 kHz. The lateral resolution was approximately 13 μm in the samples. Using this technique, mechanical properties of the phantoms were measured. The ARF excitation for producing transient excitations had previously been implemented to assess the mechanical properties of tissues [25–29]. ARF imaging had also been used in general elasticity imaging methods for the characterization of lesions, muscle screening, and imaging of the calcification of arteries [30–34].

Two types of samples were investigated in this study: an inhomogeneous tissue equivalent phantom and an *ex-vivo* bovine carotid artery embedded in gel. Four tissue equivalent phantoms with two layers were made. Each phantom was made using gelatin mixed with titanium dioxide as a scattering agent. Gelatin concentrations of 12% and 8% (indicated as high concentration and low concentration, respectively) were varied to make layers with differing stiffness values. Gelatin powder (Type B, Fisher Scientific, G7-500) and distilled water were heated in a water bath at 60–65 °C for one hour and stirred periodically. When the phantom samples cooled to 45 °C, 0.1% by weight titanium dioxide (Sigma-Aldrich,

#200332 - $15.00 USD Received 4 Nov 2013; revised 16 Jan 2014; accepted 19 Feb 2014; published 26 Feb 2014

Titanium(IV) oxide nanopowder, <25 nm particle size, 99.7% trace metals basis) was added and mixed thoroughly. The phantom solution was poured into rectangle molds (20 mm height) and allowed to congeal. The first layer was left to cool before the second layer was added on top of the first layer (as shown in Fig. 1). The inhomogeneous tissue equivalent phantom was rotated on the side and imaged.

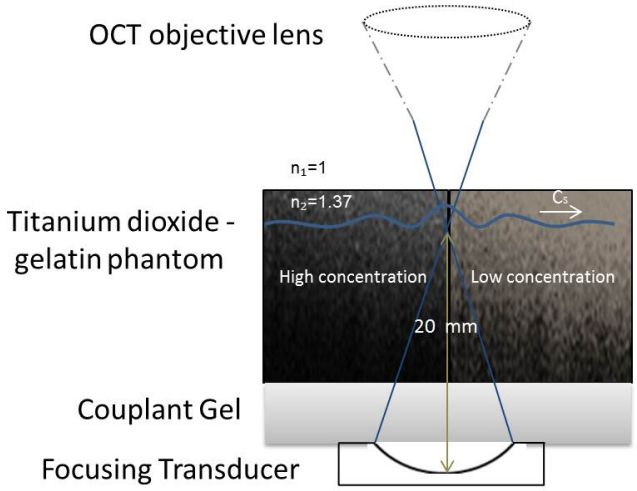

Fig. 1. A focused transducer was used to produce an ARF impulse to generate shear waves at the focal point of the transducer. The shear wave propagated in the inhomogeneous tissue equivalent phantom consisted of two layers that were labeled as hard (12% concentration) and soft (8% concentration).

A normal bovine carotid artery was obtained from a local butcher shop. The bovine carotid artery was cut into three sections and three phantoms were prepared in a similar fashion to the first phantom, but differed in the layering process. Instead of using gelatin of differing concentration as its second layer, a carotid artery sample was embedded above the first gelatin layer when the layer was cooled to 40 °C (as shown in Fig. 2). The experimental setup for the imaging of these two types of samples was described elsewhere and shown in Fig. 3 [35].

B-mode and m-mode OCT images were obtained using a commercial swept-source system (Thorlabs, Inc., USA). B-mode images of a sample (5 mm in length) were obtained at the A-scan depth of 3 mm. The focal point of the transducer for the ARF was 20 mm in depth from the transducer surface. This focal point was located 1 mm below the top surface of the sample. M-mode images of this same sample were taken along the direction of the ARF beam. In this setup, shear waves predominantly propagate radially away from the focal point in the direction perpendicular to the direction of the ARF beam.

#200332 - $15.00 USD Received 4 Nov 2013; revised 16 Jan 2014; accepted 19 Feb 2014; published 26 Feb 2014

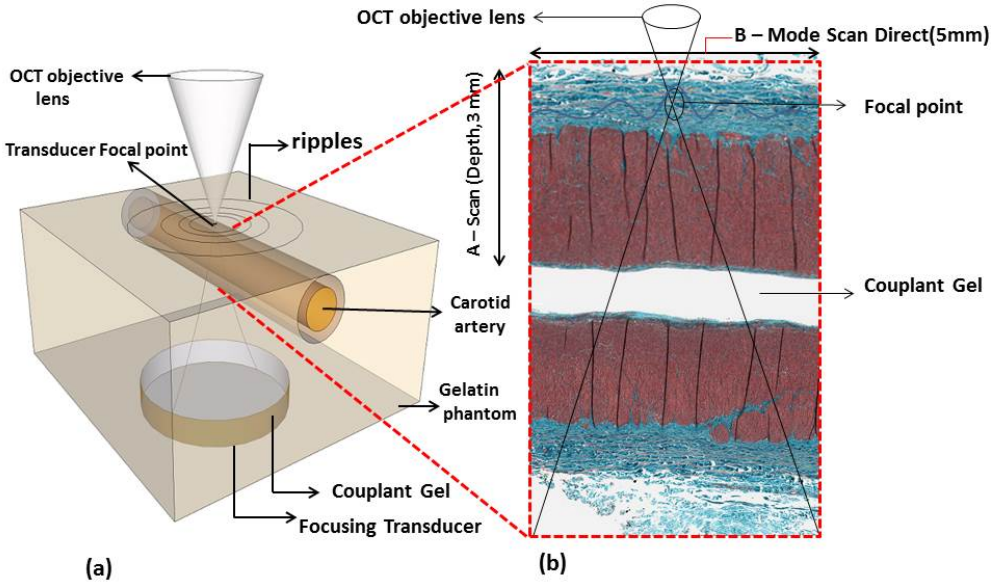

Fig. 2. **(a)** A focused transducer was used to produce an ARF impulse to generate shear waves at the focal point of the transducer, similar to Fig. 1. **(b)** The shear wave propagated in this sample consisted of the carotid artery embedded on top of the gelatin.

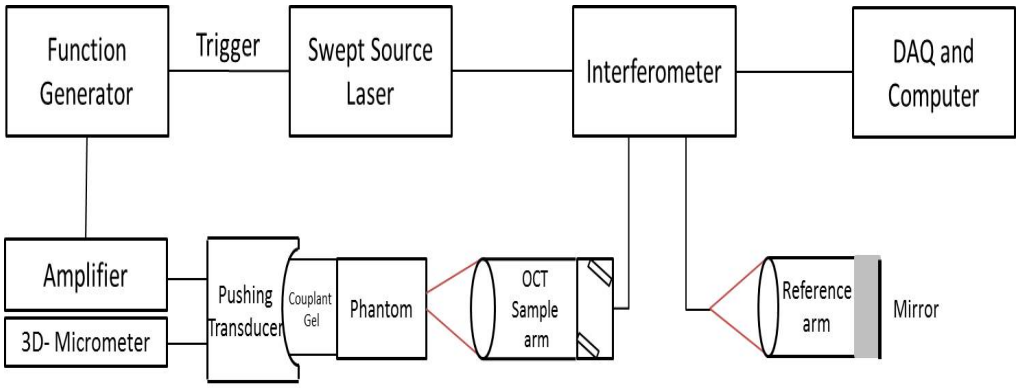

Fig. 3. A schematic diagram of the ARF-OCE experimental setup. The setup consisted of the existing SS-OCT system, an inhomogeneous titanium dioxide-gelatin phantom, a carotid artery embedded phantom, a focused pushing transducer (20 MHz, f-number 2.35), an amplifier, a 3D micrometer stage and a function generator (Agilent 33250A 80 MHz, Function / Arbitrary Waveform Generator) synchronized with the SS-OCT system.

The attenuation of shear wave was calculated by the examination of the change in signal strength in the direction of propagation of the shear wave. The attenuation of the shear wave as it propagates through the phantom is given by Eq. (1):

$$I = I_0 \exp(-\alpha x). \quad (1)$$

#200332 - $15.00 USD Received 4 Nov 2013; revised 16 Jan 2014; accepted 19 Feb 2014; published 26 Feb 2014

where I is the intensity of the shear wave that has propagated a distance x through the material, I_0 is the intensity of the shear wave at the focal spot and α is the shear wave attenuation coefficient. To calculate the attenuation coefficient, the signal strength at different locations in the phantom was obtained as a function of distance from the focal spot using the Peak displacement as an indicator of intensity (x). The amplitude of the shear wave was obtained by averaging 512 A-lines to obtain the average value for α. A best fit to the average amplitude as a function of lateral distance was obtained using the MATLAB function envelope for a lateral distance of 5 mm. From this best fit, the shear wave attenuation coefficient was calculated.

Shear wave speed can be calculated using Eq. (2):

$$C_S(\omega) = \frac{\omega \Delta r}{\Delta \varphi}. \tag{2}$$

where $\omega = 2\pi f$, $\Delta\varphi$ *is* the phase shift and Δr *is* the distance between the two successive lateral distance points. OCT images of the inhomogeneous phantoms were taken with the SS-OCT system and B-mode phase maps were obtained. These images provided information to track the phase shift (Δφ) at two successive lateral distance points (Δr) for a given depth z from which the shear wave speed was calculated. This was done for each pair of points in the image choosing the distance Δr as 0.5 mm and all pairs of points in the image. After obtaining the speed maps, they are then converted to shear modulus maps using Eq. (3):

$$C_S = \sqrt{\frac{\mu}{\rho}}. \tag{3}$$

where μ represents the shear modulus and ρ is density of the sample, resulting in Fig. 4(c).

3. Results and conclusion

OCT images of the inhomogeneous phantoms were obtained with the SS-OCT system and are shown in Fig. 4. The B-mode images, as well as their respective phase and displacement maps, allowed the calculation of distance between locations in the image, the phase shift between these locations, and the sample displacement caused by the shear wave.

#200332 - $15.00 USD Received 4 Nov 2013; revised 16 Jan 2014; accepted 19 Feb 2014; published 26 Feb 2014

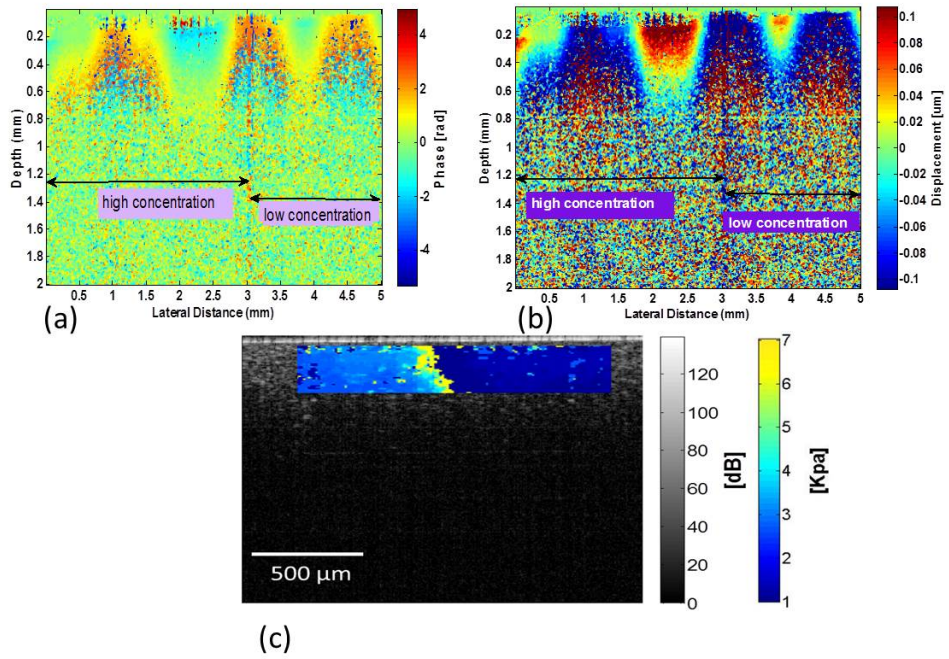

Fig. 4. **(a)** The B-mode phase map of the phantom was used to measure Δr and Δφ for the calculation of the shear wave speed. The color scale represents the change of the phase value (radians). The two layers (labeled with the arrows) had different gelatin concentrations. **(b)** Displacement of shear wave in the inhomogeneous phantom. The color bar represents the particle displacement (in µm). **(c)** B-Mode OCT structural image of the inhomogeneous titanium dioxide – gelatin phantom with a shear modulus map (color scale) superimposed on the B-mode image.

OCT images of the inhomogeneous phantoms were taken with the SS-OCT system and B-mode phase maps were obtained. These images provided information to calculate the distance between two measurement points (Δr) and the phase shift (Δφ) between these two tracking locations for each layer which two successive locations can be chosen at a particular depth z (in this work we chose z = 0.2mm in the regions of high concentration and also in the regions of low concentration). At these two locations in the image, phase values are retrieved, then were in turn used to calculate the shear wave speed, shear modulus and Young's modulus [28]. The optical path displacement *Z* is calculated from the measured phase by using Eq. (4) [36]:

$$Z = \frac{\lambda_0 \Delta\varphi}{4\pi n}. \tag{4}$$

where λ_0 is the center wavelength and *n* is the sample refractive index. In Fig. 4(b) the x-axis is the lateral distance within the phantom and the y-axis is the depth. The color in the image represents the displacement calculated from the phase maps in Fig. 4(a).

In Fig. 4(c), a shear modulus map (color scale) is superimposed on the B-mode image. The parametric images show the difference between the two sides of the phantom, with artifacts at the boundary due to the boundary discontinuity.

The image intensity along a profile through the ultrasound focus was plotted for 4 different phase offsets between the mechanical excitation and the OCT from 0 to 2π. The image intensity profiles of all phase offsets were composed in one diagram to estimate the

#200332 - $15.00 USD Received 4 Nov 2013; revised 16 Jan 2014; accepted 19 Feb 2014; published 26 Feb 2014

attenuation of the mechanical wave amplitude. Figure 5 shows a succession of images at different phase offsets illustrating the shear wave propagation in the tissue equivalent phantom.

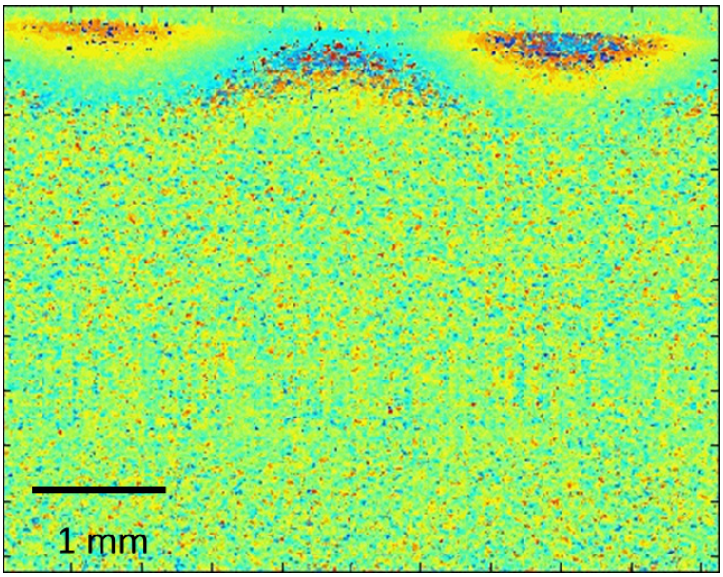

Fig. 5. A movie of the shear wave propagation (Media 1) for the tissue equivalent phantom which was created by using different phase offsets (time delays) between the Focusing Ultrasound (FUS) and OCT. The X axis and Y axis represent lateral distance(5 mm) and depth(3 mm) respectively. The color scale represent the phase, as in Fig. 4(a) (rad).

The shear wave attenuation coefficient was estimated by measuring the damping of the shear wave as it propagated away from the ARF focal spot. The focal spot was located at the boundary between the two layers of different concentrations (at around x = 3 mm in Fig. 4(a)).

The attenuation coefficient was approximately 0.8 Np/cm, which is within the range of previously published data for gelatin phantoms [37]. This was done for all four phantoms.

OCT images of three normal bovine carotid arteries samples were taken with the SS-OCT system and shown in Fig. 6.

#200332 - $15.00 USD Received 4 Nov 2013; revised 16 Jan 2014; accepted 19 Feb 2014; published 26 Feb 2014

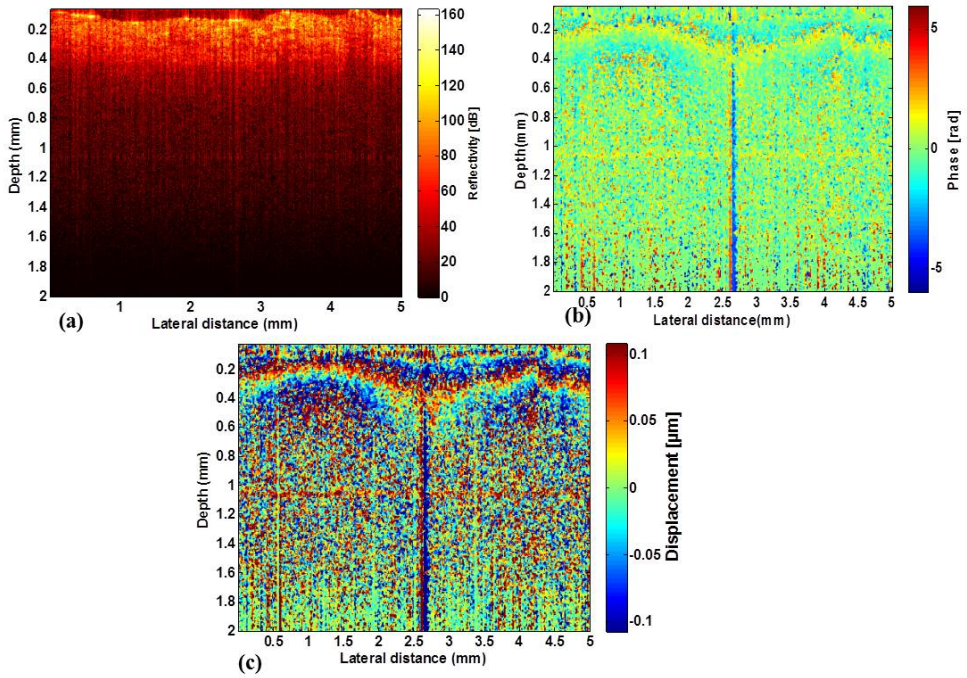

Fig. 6. B-mode OCT structural images **(a)** and the corresponding B-mode phase map **(b)** of the carotid artery samples were obtained with the SS-OCT system. The color scale represents the change of the phase value (radians). **(c)** The displacement of the sample from its initial position was measured.

After imaging with OCT, the carotid artery samples were fixed in formalin for 48 hours. Hematoxylin and Eosin (H&E) as well as Masson trichrome stains were performed, followed by whole-slide scanning (ImageScope, Aperio, Vista, CA) for quantitative digital pathology assessment of the carotid artery samples.

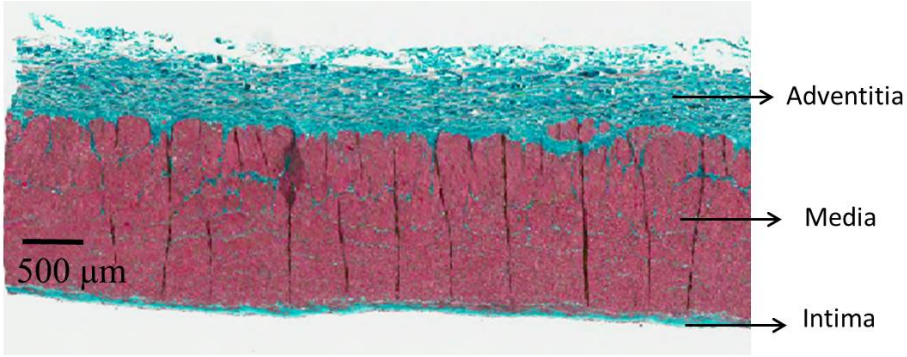

Fig. 7. Masson trichrome stain histology image of one of the *ex-vivo* carotid artery samples.

The Masson trichrome stain histology images of the *ex-vivo* carotid artery sample, shown in Fig. 7, were correlated with the phase maps of the sample. The results from these images suggest that shear waves were generated in the adventitia layer. Therefore, the mechanical properties measured are likely representative of this tissue layer.

The dominant frequency of the shear wave was calculated to be approximately 266 Hz (for both the samples). The shear wave group speed was then calculated by using the Δr and

#200332 - $15.00 USD Received 4 Nov 2013; revised 16 Jan 2014; accepted 19 Feb 2014; published 26 Feb 2014

$\Delta\varphi$ obtained from the phase map, which depicts the distance between the two measurement locations and the calculated phase shift, respectively. These values were used to calculate the shear modulus and young modulus [35]. The mechanical properties of the inhomogeneous phantoms and carotid artery samples are shown in Table 1. The average values and standard deviations were calculated from 10 different pairs of locations in the phase maps for all calculations of Δr and $\Delta\varphi$. The errors for the SW-OCE results represent the standard deviation of these 10 measurements, for all 4 phantoms. The three phantoms with the bovine carotid arteries were imaged, and the results report the average and standard deviation of the 3 measurements. As expected, the values of the Young's moduli and shear moduli were greater for the part of the phantom with the higher concentration of gelatin [35, 38]. The shear modulus and young modulus of carotid artery sample were 45.3 ± 0.6 kPa and 135.8 ± 1.8 kPa respectively.

Table 1. The mechanical properties of the inhomogeneous phantoms and carotid artery samples (adventitia). The errors for the SW-OCE results represent the standard deviation as explained in the text.

Samples	Shear wave speed (C_s, *m/s*)	Shear modulus (μ,*kPa*)	Young's modulus (E, *kPa*)
inhomogeneous phantom (high concentration, 12%)	1.87 ± 0.06	3.7 ± 0.2	11.0 ± 0.6
inhomogeneous phantom (low concentration, 8%)	1.49 ± 0.05	2.3 ± 0.1	7.0 ± 0.3
Carotid artery sample (adventitia)	5.90 ± 0.08	45.3 ± 0.6	135.8 ± 1.8

While many factors contribute, the phase stability of our OCT system during these imaging sessions are primarily affected by the signal-to-noise ratio (SNR). Therefore, we measured the phase stability as function of the SNR (Fig. 8), analogous to our previous work [39].

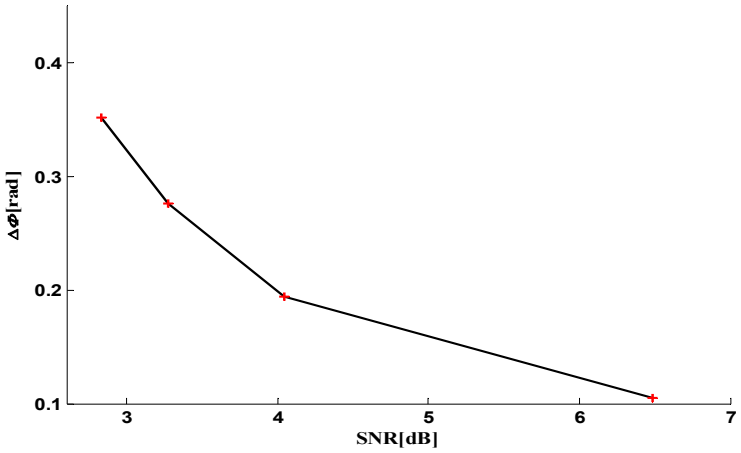

Fig. 8. Mean background phase noise (Δφ) at four different SNR regions.

4. Discussion

Shear waves were generated in inhomogeneous phantoms and in carotid artery samples. The shear modulus and Young's modulus were measured. We have demonstrated, for the first time, a SW-OCE technique that uses ARF for the mechanical excitation of a carotid sample to measure the shear modulus and Young's modulus of the adventitia. The mechanical

#200332 - $15.00 USD Received 4 Nov 2013; revised 16 Jan 2014; accepted 19 Feb 2014; published 26 Feb 2014

excitation produces motions within the sample that can be used for the estimation of mechanical properties using SW-OCE. This study demonstrated the feasibility of shear wave OCE measurements in layered media. For the tissue equivalent phantoms, we have shown how measurements of mechanical properties can be made to differentiate between the boundaries of two media with different stiffness (Fig. 4). A parametric map of the shear modulus clearly shows the difference in the shear modulus in the low and high gel concentration regions (Fig. 4(c)). It is expected that such differences in mechanical properties will occur at the transition region between a normal and diseased artery wall.

Moreover, in the carotid measurements presented in this paper, the data collected suggest that the shear waves produced were confined to the adventitia of the carotid artery. This is due to the limited penetration depth of the OCT imaging and the 10 μm axial resolution that can be achieved with this imaging modality. The values measured in Table 1 compare well to published values using different techniques such as B-mode echography [40], intravascular ultrasound [41]. Young's modulus measurements for the carotid artery lie between 30.1 ± 10.8 kPa and 614 ± 35 kPa, and depend on many parameters such as species, age, diameter and disease [40]. The measurement of the elastic properties of the adventitia demonstrates how the superior spatial resolution of OCT can be used in the SW-OCE approach to interrogate tissue structures that are too small to be resolved with other competing imaging methods.

Tissue elasticity may be thought of simply as the relative hardness or softness of a biomaterial, and clinical examination by palpation is a traditional and highly effective means of detecting pathologies such as coronary artery disease, which demonstrates local elastic inhomogeneity. OCT provides greater spatial and phase resolution than previous methods that have been used for the study of the deformation of tissue and biomaterials. The spatial resolution of mechanical property maps will depend on whether reliable phase difference measurements between locations can be made with SW-OCE. It is expected that these maps have much better spatial resolution compared to the shear wave wavelength.

Acknowledgments

Marjan Razani is supported by a Natural Sciences and Engineering Research Council of Canada (NSERC) Doctoral Scholarship. This work is funded in part by the Canada Research Chairs program (awarded to Drs. V.X.D. Yang and M. C. Kolios), the Natural Sciences and Engineering Research Council of Canada (NSERC Discovery Grant 216986-2012) and the Canada Foundation for Innovation. We would like to thank Dr. Mathias Fink for his contributions and discussions.

#200332 - $15.00 USD Received 4 Nov 2013; revised 16 Jan 2014; accepted 19 Feb 2014; published 26 Feb 2014